JACS
JOURNAL OF THE AMERICAN CHEMICAL SOCIETY
Article
Cite This: J. Am. Chem. Soc. 2018, 140, 17040−17050
pubs.acs.org/JACS

Hemilabile Proton Relays and Redox Activity Lead to {FeNO}^{x} and Significant Rate Enhancements in NO_2^- Reduction

Pui Man Cheung,[†] Kyle T. Burns,[†] Yubin M. Kwon,[†] Megan Y. Deshaye,[†] Kristopher J. Aguayo,[†] Victoria F. Oswald,[§] Takele Seda,[⊥] Lev N. Zakharov,[‡] Tim Kowalczyk,*[,†] and John D. Gilbertson*[,†]

[†]Department of Chemistry and [⊥]Physics, Western Washington University, Bellingham, Washington 98225, United States
[‡]Department of Chemistry, University of Oregon, Eugene, Oregon 97403, United States
[§]Department of Chemistry, University of California, Irvine, Irvine, California 92697, United States

Supporting Information

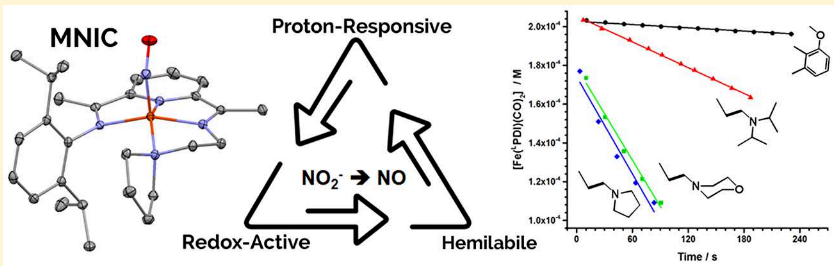

ABSTRACT: Incorporation of the triad of redox activity, hemilability, and proton responsivity into a single ligand scaffold is reported. Due to this triad, the complexes Fe(^{Pyrr}PDI)$(CO)_2$ (**3**) and Fe(^{Mor}PDI)$(CO)_2$ (**4**) display 40-fold enhancements in the initial rate of NO_2^- reduction, with respect to Fe(^{MeO}PDI)$(CO)_2$ (**7**). Utilizing the proper sterics and pK_a of the pendant base(s) to introduce hemilability into our ligand scaffolds, we report unusual {FeNO}^{x} mononitrosyl iron complexes (MNICs) as intermediates in the NO_2^- reduction reaction. The {FeNO}^{x} species behave spectroscopically and computationally similar to {FeNO}^{7}, an unusual intermediate-spin Fe(III) coupled to triplet NO^- and a singly reduced PDI ligand. These {FeNO}^{x} MNICs facilitate enhancements in the initial rate.

■ INTRODUCTION

In addition to the physiological role in the regulation of nitric oxide (NO) in mammalian blood flow,[1,2] nitrite (NO_2^-) plays an integral role in the global nitrogen cycle.[3,4] While NO_3^- composes the majority of species in water runoff, the two-proton, one-electron reduction of NO_2^- to NO is a vital step in the removal of nitrogen oxides in the treatment of municipal water,[5] as the overuse of fertilizers rich in nitrogen is responsible for the presence of toxic levels of NO_2^- (and NO_3^-) in water runoff.[4,6] Biological NO_2^- reduction ($NO_2^- + 2H^+ + e^- \rightarrow NO + H_2O$) occurs in nitrite reductase (NiR) enzymes[3] and also hemoglobin,[7,8] myoglobin,[9,10] cytochrome P450, cytochrome *c*, and nitric oxide synthase.[11,12] Additionally, postulated mechanisms of nitrite reduction by cytochrome *cd*$_1$ NiRs include the formation of weakly bound {FeNO}^{x} species.[2,13−17]

As in the case of NO_2^- reduction, many important biological reactions occur by managing the proton and electron flow at the enzyme active site.[18−20] To this end, there has been a resurgence into redox-active,[21,22] hemilabile,[23−27] and so-called proton-responsive ligand scaffolds.[28−40] However, studies that incorporate the triad of redox activity, hemilability, and proton responsivity, all in a single ligand scaffold, are exceedingly limited.[41−47] Our group has been active in developing methodologies that control the movement of both protons and electrons for biologically relevant reactions by utilizing the redox-active pyridinediimine (PDI) scaffold merged with a proton-responsive secondary coordination sphere.[48−50] Those preliminary studies successfully showed (1) the PDI scaffold can be tailored to facilitate NO_2^- reduction and (2) the NO_2^- reduction is dependent on the protonation state of the secondary coordination sphere (proton responsivity). Furthermore, given the revelations of the role ligand hemilability plays in biomimicry,[51−53] we reasoned that the pendant base(s) could be utilized to introduce hemilability into the PDI, yielding ligand scaffolds that increase activity even further. We describe here our efforts toward encompassing the triad, utilizing the proper sterics and pK_a of the pendant base(s) to introduce hemilability into our ligand scaffolds. Through the isolation of novel mononitrosyl {FeNO}^{x} species, we demonstrate that ligand hemilability, when integrated with redox activity and proton responsivity, is responsible for significant enhancements in the initial rate of NO_2^- reduction (~40×) compared to the systems that are not integrated.

Received: August 8, 2018
Published: November 14, 2018

DOI: 10.1021/jacs.8b08520
J. Am. Chem. Soc. 2018, 140, 17040−17050

■ RESULTS AND DISCUSSION

Synthesis and Characterization of Fe(PDI) Complexes. The target PDI ligands in this study were the pyrrolidine (^{Pyrr}PDI) and morpholine (^{Mor}PDI) analogues, given their minimal steric bulk and favorable pK_a range in CH_3CN (free pyrrolidine = 19.6 and free morpholine = 16.6).[54,55] As shown in eq 1, the direduced $Fe(PDI)(CO)_2$

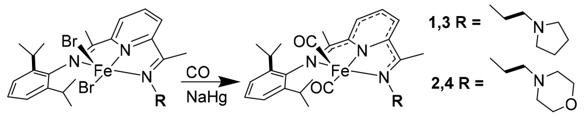

(1)

complexes, Fe(^{Pyrr}PDI)$(CO)_2$ (**3**) and Fe(^{Mor}PDI)$(CO)_2$ (**4**), were synthesized from the NaHg reduction of the dihalide precursosrs Fe(^{Pyrr}PDI)Br_2 (**1**) and Fe(^{Mor}PDI)Br_2 (**2**) in CH_2Cl_2 under an atmosphere of CO.

Evaporation of saturated diethyl ether solutions of either **3** or **4** yields green, diamagnetic crystalline solids, which display ν_{CO} stretches in the ATR-FTIR spectra at 1942 and 1876 cm^{-1} for **3** and 1934 and 1871 cm^{-1} for **4**. The solid-state structures of **3** and **4** are shown in Figure 1. The iron center in both

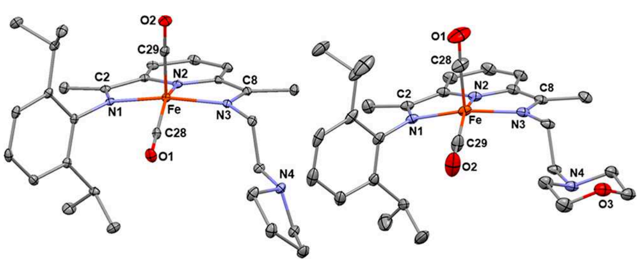

Figure 1. Solid-state structures (30% probability) of Fe(^{Pyrr}PDI)-$(CO)_2$ (**3**, left) and Fe(^{Mor}PDI)$(CO)_2$ (**4**, right). The H atoms have been omitted for clarity. Selected bond lengths (Å) and angles (deg) for **1**: Fe(1)−C(28) 1.784(1), Fe(1)−C(29) 1.782(2), Fe(1)−N(1) 1.944(1), Fe(1)−N(2) 1.849(1), Fe(1)−N(3) 1.948(2), C(2)−N(1) 1.332(2), C(8)−N(3) 1.324(2) and C(28)Fe(1)C(29) 95.65(7), N(2)Fe(1)C(28) 153.81(7), N(1)Fe(1)N(3) 154.16(6). Selected bond lengths (Å) and angles (deg) for **2**: Fe(1)−C(28) 1.780(2), Fe(1)−C(29) 1.769(2), Fe(1)−N(1) 1.954(1), Fe(1)−N(2) 1.851(1), Fe(1)−N(3) 1.953(1), C(2)−N(1) 1.332(2), C(8)−N(3) 1.332(2) and C(28)Fe(1)C(29) 97.62(9), N(2)Fe(1)C(29) 156.22(7), N(1)Fe(1)N(3) 153.42(5).

complexes is five coordinate with square pyramidal geometry (τ = 0.01 in **3** and 0.05 in **4**).[56] The C_{imine}−N_{imine} bond lengths in **3** (1.332(2) and 1.324(2) Å) and **4** (1.332(2) and 1.323(2) Å), coupled with the C_{imine}−C_{ipso} bond lengths (1.426(2) and 1.438(2) Å in **3** and 1.423(2) and 1.434(2) Å in **4**), are indicative of a doubly reduced PDI ligand bound to an $S = 0$ Fe(II) center. The room-temperature zero-field Mössbauer parameters ($\delta = -0.089(3)$, $\Delta E_Q = 1.197(3)$ mm/s in **3** and $\delta = -0.08(1)$, $\Delta E_Q = 1.46(2)$ mm/s in **4**) support these assignments.

Similar to the previously reported Fe(didpa)$(CO)_2$ (didpa = [(2,6-^{i}PrC_6H_3)(N═CMe)(N(^{i}Pr)$_2C_2H_4$)(N═CMe)-C_5H_3N]) complex,[50] **3** and **4** both react with two equivalents of NO_2^- and four equivalents of H^+ yielding the representative dinitrosyl iron complexes (DNICs) [Fe(^{Pyrr}PDI)$(NO)_2$]$^+$ (**5**) and [Fe(^{Mor}PDI)$(NO)_2$]$^+$ (**6**). The solid-state structures of **5** and **6** are shown in Figure 2. The iron center in each complex is five-coordinate, distorted square pyramidal (τ = 0.24 in **5** and τ = 0.32 in **6**). The PDI backbone is in the neutral form,

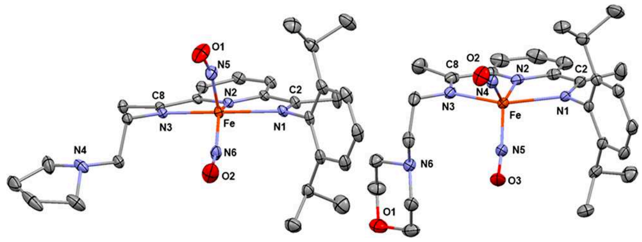

Figure 2. Solid-state structures (30% probability) of [Fe(^{Pyrr}PDI)-$(NO)_2$]$^+$ (**5**, left) and [Fe(^{Mor}PDI)$(NO)_2$]$^+$ (**6**, right). The H atoms and the BPh_4^- counterion have been omitted for clarity. Selected bond lengths (Å) and angles (deg) for **5**: Fe(1)−N(1) 2.216(2), Fe(1)−N(2) 2.080(1), Fe(1)−N(3) 2.138(2), Fe(1)−N(5) 1.693(2), Fe(1)−N(6) 1.696(2), N(1)−C(2) 1.285(2), N(3)−C(8) 1.283(2) and N(5)−Fe(1)−N(6) 108.7(1), N(2)−Fe(1)−N(6) 132.85(8), N(1)−Fe(1)−N(3) 147.38(6). Selected bond lengths (Å) and angles (deg) for **6**: Fe(1)−N(1) 2.233(3), Fe(1)−N(2) 2.065(2), Fe(1)−N(3) 2.171(3), Fe(1)−N(4) 1.694(2), Fe(1)−N(5) 1.696(3), N(1)−C(2) 1.280(3), N(3)−C(8) 1.290(3) and N(4)−Fe(1)−N(5) 108.6(1), N(2)−Fe(1)−N(4) 128.9(1), N(1)−Fe(1)−N(3) 148.23(9).

confirming the ligand-based reduction of NO_2^-, as evidenced by the contracted C_{imine}−N_{imine} bonds (1.283(2) and 1.285(2) Å in **5**; 1.280(3) and 1.290(3) Å in **6**) and the elongated C_{imine}−C_{ipso} bonds (1.488(3) and 1.488(3) Å in **5**; 1.486(4) and 1.483(5) Å in **6**). The average Fe−N(O) bond lengths in both **5** and **6** are 1.695 Å, and the average N−O bond lengths are 1.172 Å in **5** and 1.167 Å in **6**. The Fe−N−O units are slightly bent in both complexes in an "attracto" conformation[57] with average Fe−N−O angles of 161.1° in **5** and 161.5° in **6**. As in our previously reported DNICs on the PDI scaffold, the Enemark−Feltham notation[58] that best describes both **5** and **6** is $\{Fe(NO)_2\}^9$. Both complexes exhibit ν_{NO} stretches in the ATR-FTIR spectra at 1785 and 1716 cm^{-1} for **5** and 1783 and 1709 cm^{-1} for **6** (Figures S10 and S11). These stretches shift to 1752 and 1682 cm^{-1} and 1749 and 1677 cm^{-1}, respectively, upon isotopic substitution with ^{15}NO. Both **5** and **6** exhibit the characteristic $S = 1/2$ EPR signal at $g = 2.01$ (Figure S20) observed for $\{Fe(NO)_2\}^9$ DNICs.[59]

Proton Responsivity and Kinetics of NO_2^- Reduction. Previously we have shown that the pendant base in Fe(PDI)$(CO)_2$ complexes plays a crucial role in facilitating NO_2^- reduction.[49,50] In order to probe the role of the pendant base in the NO_2^- reduction reaction in depth, we performed a series of kinetic experiments comparing the initial rates.[60] All nitrite reductions were run in CH_3CN with $TBANO_2$ as the source of soluble NO_2^-. We chose Fe(^{MeO}PDI)$(CO)_2$ (**7**) (where ^{MeO}PDI = [(2,6-^{i}PrC_6H_3)N═CMe)(2-MeO-6-MeC_6H_3)N═CMe)C_5H_3N])[61] as the control compound to compare initial rates, as it does not contain a pendant base but is active in NO_2^- reduction.[62] The pK_a of the pendant pyrrolidine in **3** was measured to be 18.3 (CH_3CN), and the pendant morpholine in **4** was measured to be 17.1 (CH_3CN). These values mirror the values for pyrrolidine (19.6)[54] and morpholine (16.6).[55] We also included Fe(didpa)$(CO)_2$ (**8**) in the kinetic analysis, given its bulkier diisopropylamine pendant base with a similar pK_a (19.2)[48] to **3**.

As shown in the top plot in Figure 3 when $[HNEt_3]^+$ (pK_a = 18.8 in CH_3CN)[54] is used as the acid source, the initial rate of 2.11×10^{-8} M s^{-1} is observed for the control compound, **7** (Table 1). An increase in initial rate of ~2× (3.97×10^{-8} Ms^{1-}) is observed for **8** and ~3× (7.07×10^{-8} M s^{-1}) is

DOI: 10.1021/jacs.8b08520
J. Am. Chem. Soc. 2018, 140, 17040−17050

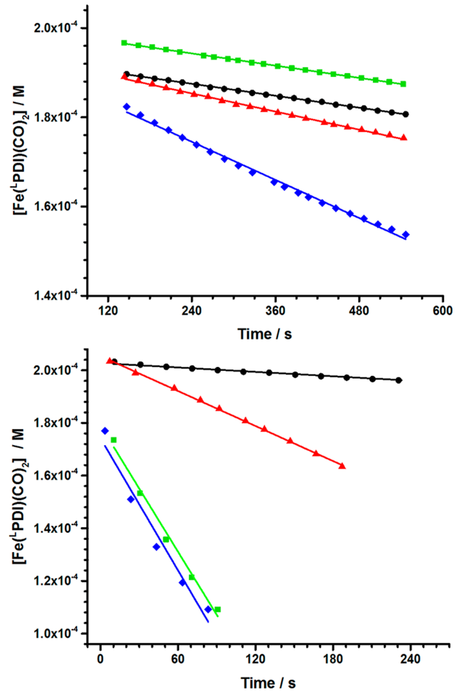

Figure 3. Initial rate plots for the reduction of $TBANO_2$ by selected Fe(PDI)(CO) species and 4 equiv of $[HNEt_3]^+$(top) and $[HLut]^+$ (bottom). Black circles = **7**, red triangles = **8**, blue diamonds = **3**, and green squares = **4**.

observed for **3**. However, virtually no increase (2.30×10^{-8} M s^{-1}) is observed for **4**. These results can be explained, in part, by examination of the pK_a of the pendant base, which in the case of both **8** and **3** are both in the range for proton transfer from $[HNEt_3]^+$. Compound **4**'s pK_a is too low to be protonated by $[HNEt_3]^+$ to any appreciable extent, effectively eliminating the proton shuttling capability of the pendant base. As shown in Figure 3 (bottom), when the acid source is changed to $[HLut]^+$ (where Lut = 2,6-dimethylpyridine), which has a pK_a = 14.1 in CH_3CN,[54] the rates observed for both **3** and **4** are virtually identical (8.11×10^{-7} M s^{-1} and 8.45×10^{-7} M s^{-1}, respectively), illustrating that $[HLut]^+$ is a strong enough acid to protonate the pendant morpholine group in **4** for proton shuttling. Furthermore, that corresponds to a ~*40-fold rate enhancement* for these compounds compared to **7**, whose initial rate is unaffected by utilization of the stronger acid (2.52×10^{-8} M s^{-1}).

Role of Hemilability and the Isolation of $\{FeNO\}^x$ MNICs. This begs the question, why then does **8** not display a similar rate enhancement? As shown in Table 1, NO_2^- reduction by **8** with $[HLut]^+$ does result in a rate enhancement (as would be expected given the stronger acid source), but only a 10-fold increase in initial rate is observed, significantly less than the ~40-fold enhancement exhibited by both **3** and **4**. The answer lies in the fact that the diisopropylamine of **8** is not hemilabile (due to the sterics of the isopropyl groups on the amine). The hemilability of the pendant pyrrolidine and morpholine groups is clearly illustrated by the isolation of the mononitrosyl intermediates $[Fe(^{Pyrr}PDI)(NO)]^+$ (**9**) and $[Fe(^{Mor}PDI)(NO)]^+$ (**10**), in which the pendant base of each complex is coordinated to the iron center. These mononitrosyl iron complexes (MNICs) can be synthesized independently from either **3** or **4** with only one equivalent of NO_2^- and two equivalents of H^+ (eq 2):

$$Fe(PDI)(CO)_2 + NO_2^- + 2H^+ \rightarrow [Fe(PDI)(NO)]^+ + H_2O + 2CO \quad (2)$$

As shown in Figure 4, the iron center in each complex is five-coordinate, square pyramidal (τ = 0.09 in **9** and τ = 0.12 in **10**)

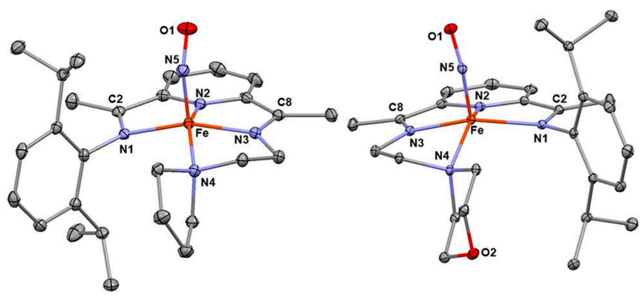

Figure 4. Solid-state structures (30% probability) of $[Fe(^{Pyrr}PDI)(NO)]^+$ (**9**, left) and $[Fe(^{Mor}PDI)(NO)]^+$ (**10**, right). The H atoms and the BPh_4^- counterion have been omitted for clarity. Selected bond lengths (Å) and angles (deg) for **9**: Fe(1)−N(1) 2.031(1), Fe(1)−N(2) 1.830(2), Fe(1)−N(3) 1.894(1), Fe(1)−N(4) 2.066(1), Fe(1)−N(5) 1.677(2), N(1)−C(2) 1.315(2), N(3)−C(8) 1.313(2) and N(5)−Fe(1)−N(4) 104.09(7), N(2)−Fe(1)−N(4) 152.92(7), N(1)−Fe(1)−N(3) 147.66(6). Selected bond lengths (Å) and angles (deg) for **10**: Fe(1)−N(1) 2.035(1), Fe(1)−N(2) 1.836(1), Fe(1)−N(3) 1.894(1), Fe(1)−N(4) 2.076(1), Fe(1)−N(5) 1.679(1), N(1)−C(2) 1.314(1), N(3)−C(8) 1.313(2) and N(4)−Fe(1)−N(5) 104.59(5), N(2)−Fe(1)−N(4) 144.87(4), N(1)−Fe(1)−N(3) 151.92(4).

Table 1. Selected Initial Rates of $TBANO_2$ Reduction[a]

compound (pK_a)	rate 1[b] ($\times 10^{-8}$ M s^{-1})	rate 2[c] ($\times 10^{-8}$ M s^{-1})	rate[d] relative to 7
7 (—)	2.11	2.52	1.00 (1.19)
3 (18.3)	7.07	81.1	3.35 (38.42)
4 (17.1)	2.30	84.5	1.09 (40.01)
8 (19.2)	3.97	21.2	1.88 (10.06)

[a]25 °C, 2 equiv of $TBANO_2$, 4 equiv of H^+, CH_3CN. [b]Average, $[HNEt_3]^+$. [c]Average, $[HLut]^+$. [d]Rate 1 (rate 2).

with the hemilabile pendant group now part of the primary coordination sphere of the iron center. The PDI backbone in both complexes is still in a reduced form, as evidenced by the $C_{imine}-N_{imine}$ bonds (1.315(2) and 1.313(2) Å in **9**; 1.314(1) and 1.313(2) Å in **10**) and the $C_{imine}-C_{ipso}$ bonds (1.453(2) and 1.439(2) Å in **9**; 1.446(2) and 1.440(2) Å in **10**). The Fe−N(O) bond lengths in **9** and **10** are 1.677(2) and 1.679(1) Å, respectively, where the N−O bond length in **9** is 1.182(2) Å and in **10** is 1.183(2) Å. The Fe−N−O angle in **9** is 150.9(2)° and in **10** is 154.4(1)°. Both complexes are diamagnetic in the solid state and solution (Evan's method) and exhibit a single ν_{NO} stretch in the ATR-FTIR spectrum at 1667 cm^{-1} for **9** and 1687 cm^{-1} for **10** (Figures S15 and S19) that shifts to 1635 and 1654 cm^{-1}, respectively, upon isotopic substitution with ^{15}NO.

The MNIC **9** (and also **10**) is an isolated intermediate along the nitrite reduction reaction coordinate (Figure S26), evidenced by the fact that the DNIC **5** can be produced in quantitative yield from the addition of one equivalent of NO_2^- and two equivalents of H^+ to solutions of **9**. Inspection of the solution FTIR spectra (Figure S27) of the reaction mixtures

DOI: 10.1021/jacs.8b08520
J. Am. Chem. Soc. 2018, 140, 17040−17050

reveals the disappearance of the ν_{NO} band at 1667 cm^{-1} for **9** and the appearance of the ν_{NO} bands at 1785 and 1716 cm^{-1} for **5**. Additionally, the UV−vis spectrum of independently prepared **9** is identical to the spectrum obtained at the inflection point in the global kinetic trace of the reaction of **3** with two equivalents of NO_2^- and four equivalents of H^+ (Figure S21). There are also well-anchored isosbestic points at 522 and 650 nm in the stacked UV−vis reaction plots, indicating clean formation of one product (**9**). From these data it is clear that formation of the MNIC intermediate is essential and that these hemilablile ligands facilitate the propensity of NO_2^- reduction (Scheme 1).

Scheme 1. Reduction of NO_2^-, Illustrating the Role of the Hemilabile Pendant Base

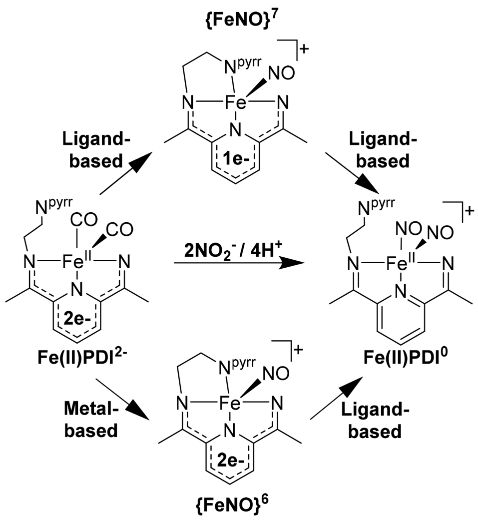

Redox Activity and the $\{FeNO\}^x$ Enemark−Feltham Notation. The Enemark−Feltham notation that best describes **9** (and also **10**) is somewhat ambiguous. The PDI ligand in **9** is in a reduced form (see above), and the room-temperature zero-field Mössbauer parameters (δ = 0.094(3), ΔE_Q = 0.489(5) mm/s) in **9** suggest that the iron center in **9** is more oxidized than the Fe(II) center in the DNIC, **5** (δ = 0.32(3), ΔE_Q = 0.82(9) mm/s).[63] Given that **9** is diamagnetic, one could assign the oxidation state(s) as Fe(III), antiferromagnetically coupled to a $NO^\bullet$ radical ligand (confirmed by the Fe−N−O angle of 150.9(2)°)[64] and PDI^{2-}. This would result in an Enemark−Feltham notation of $\{FeNO\}^6$.

If the MNIC **9** (and also **10**) is $\{FeNO\}^6$, then the bent NO is very unusual. To the best of our knowledge, there are no reported examples of five-coordinate S=0 $\{FeNO\}^6$ species with a bent NO ligand. Typically, the Fe−N−O linkage found in $\{FeNO\}^6$ species is linear.[65,66] Virtually all iron nitrosyls reported to date obey this rule, with the exception of the six-coordinate $\{FeNO\}^6$ ferric complex (OEP)Fe(NO)(*p*-C_6H_4F)[67] (where OEP = octaethylporphyrinato dianion), which displays an Fe−N−O angle of 157.4° and a ν_{NO} stretch of 1791 cm^{-1}, and nitrophorin 4, a salivary protein of the blood-sucking insect *Rhodnius prolixus* (Fe−N−O angle = 156°).[68]

The ν_{NO} stretch observed for **9** (1667 cm^{-1}) and **10** (1687 cm^{-1}) is also significantly lower than the characteristic range for six- and even five-coordinate $\{Fe(NO)\}^6$ complexes.[69−72] In addition, the especially low Fe−N−O angles (150.9(2)° in **9** and154.4(1)° in **10**) are closer to the range of the more electron rich $\{Fe(NO)\}^7$ complexes,[73] where either the Fe(II)-$NO^\bullet$ radical or Fe(III)-NO^- description would be more appropriate. This description, coupled with the fact that both complexes are diamagnetic, suggests that the PDI ligand is also likely a monoradical (see computations below). As stated above, the PDI ligand in **9** (and **10**) is in the reduced form, but it is difficult to distinguish between PDI^{2-} and/or the PDI^- (monoradical) state using crystallographic data. For example, the C_{imine}−N_{imine} bonds in **9** are slightly shorter (0.017 Å) than **3**, and the C_{imine}−C_{ipso} bonds are slightly longer (0.027 Å), suggesting it may be more oxidized (Table 2). If **9** had more

Table 2. Selected Spectroscopic and Crystallographic Data for Fe(PDI) Complexes[a]

	3	9	5	$9^{(2,2)}$[b]
C(2)−N(1)	1.332(2)	1.315(2)	1.285(2)	1.302
C(8)−N(3)	1.32(4)	1.313(2)	1.283(2)	1.314
C(2)−C(3)	1.426(2)	1.453(2)	1.488(3)	1.450
C(7)−C(8)	1.438(2)	1.439(2)	1.488(3)	1.432
Fe(1)−N(1)	1.944(1)	2.031(1)	2.216(2)	2.060
Fe(1)−N(2)	1.849(1)	1.830(2)	2.080(1)	1.839
Fe(1)−N(3)	1.948(2)	1.894(1)	2.138(2)	1.899
Fe(1)−N_{pyrr}(4)		2.066(1)		2.101
Fe(1)−N(5)(O)		1.677(2)	1.693(2)	1.747
Fe(1)−N(6)(O)			1.696(2)	
N(5)−O(1)		1.182(2)	1.170(3)	1.167
N(6)−O(2)			1.173(3)	
Fe−N(5)−O(1)		150.9(2)	161.9(2)	147.5
Fe−N(6)−O(2)			160.4(2)	
ν_{NO}(cm^{-1})		1667	1785, 1716	
S	0	0	1/2	0
δ (mm/s)	−0.089(3)	0.094(3)	0.32(3)	
ΔE_Q (mm/s)	1.197(3)	0.489(5)	0.82(9)	

[a]Bond lengths (Å) and angles (deg). [b]BS(2,2) solution.

Fe(II)-PDI^- character, with only one electron-withdrawing NO ligand, this could account for both the slight differences in bond lengths and higher isomer shift (0.094(3) for **9** and −0.089(3) for **3**), given the strongly electron withdrawing CO ligands in **3**. However, it should be noted that there are no reported diamagnetic $\{Fe(NO)\}^7$ complexes.

Lastly, given that in some direduced FePDI complexes[74,75] the PDI ligand can be described as a resonance hybrid between a PDI^0 and PDI^{2-}, an ambiguous electronic structure with contributions from both $\{FeNO\}^6$ and $\{FeNO\}^8$ configurations may be appropriate (see electronic structure calculations below). This would result in some contribution from the Fe(I)-$NO^\bullet$ radical nature of the NO ligand in **9**. $\{FeNO\}^8$ complexes are S = 0, but typically possess an NO^- ligand with a much lower Fe−N−O bond angle and ν_{NO} stretch than observed in **9** and **10**.[65]

Depending on the $\{FeNO\}^x$ description, the first NO_2^- reduction in Scheme 1 can be described as either a one-electron metal-based event yielding $\{FeNO\}^6$ (Scheme 1, bottom) or a ligand-based event yielding $\{FeNO\}^7$ (Scheme 1, top). The second NO_2^- reduction in either case is then ligand-based, yielding the $\{Fe(NO)_2\}^9$ DNIC. If the intermediate MNIC is $\{FeNO\}^6$, then the second, ligand-based event would include two electrons from the PDI, one to reduce the iron center and the other to reduce the second NO_2^-, forming the

DOI: 10.1021/jacs.8b08520
J. Am. Chem. Soc. 2018, 140, 17040−17050

corresponding Fe(II)PDI^0 DNIC.[76] Regardless of the electronic description of **9** and **10**, the hemilabile, proton-responsive secondary coordination sphere is absolutely vital for the rate accelerations.

Electronic Structure Calculations. In order to complement experiment, **3**, **5**, and **9** were investigated computationally. Specifically, broken-symmetry density functional theory (BS-DFT) energies and optimized geometries were evaluated. Initial guess wave functions for BS calculations were prepared through a spin-flip on iron from a high-spin reference Kohn–Sham (KS) determinant. The notation BS(m,n) was adopted to represent a broken-symmetry solution with m unpaired electrons on iron antiferromagnetically coupled to n unpaired electrons on the ligands. The unpaired spin-down electron density was not forced to localize on the PDI or NO ligand specifically.

The electronic structure of **3** was initially computed, given that previous analyses of the closed-shell frontier orbitals of direduced Fe(PDI)$(CO)_2$ complexes suggest that they are best represented as a resonance hybrid of a PDI^0 ligand on a Fe(0) d^8 center and a PDI^{2-} ligand on a low-spin Fe(II) center.[74,75] We computed the closed-shell BS(0,0) wave function for **3**, and the results are in agreement with the previous studies. The HOMO, shown in Figure S28, is distributed across both the iron center and the PDI ligand, reinforcing the notion that the ground-state electronic structure is a hybrid of Fe(0) and Fe(II) with significant metal–ligand covalent character. We also obtained a BS(2,2) wave function for **3**, which yielded an electronic energy 1.8 kcal/mol below that of the BS(0,0) solution at the BS(2,2)-optimized geometry. This gap decreases to 0.8 kcal/mol at the BS(0,0)-optimized geometry. The BS(2,2) solution qualitatively resembles an intermediate-spin Fe(II) center antiferromagnetically coupled to a triplet PDI^{2-} ligand. However, with such a small energy gap, both states are expected to be thermally accessible at room temperature.

The lowest-energy electronic configuration computed for the DNIC, **5**, was the $S = 1/2$ configuration; our efforts toward the $S = 3/2$ configuration failed to converge. The $S = 1/2$ configuration can be considered a resonance hybrid in which each resonance form consists of one formal NO anion and one formal NO radical antiferromagnetically coupled to an intermediate-spin Fe(II) center; the PDI ligand is formally neutral in this configuration.[77] The frontier orbitals of **5** in Figure S29 show that none of the highest-occupied MOs have a significant contribution from the PDI ligand, supporting a neutral assignment for PDI in this complex and an overall assignment of $\{Fe(NO)_2\}^9$PDI^0. The spin density (Figure S30) is mostly localized to the nitrosyl ligands and iron center. These results are in agreement with previously reported $\{Fe(NO)_2\}^9$ DNICs.[78,79]

For **9**, the redox noninnocence of both the NO and PDI ligand results in a range of plausible oxidation and spin states for the complex. Assignments ranging from $\{FeNO\}^6$ through $\{FeNO\}^8$ are possible depending on whether the PDI ligand is formally doubly, singly, or not reduced, respectively. Furthermore, the multireference character observed in other Fe-PDI complexes[80] hints at the possibility that a single electronic configuration may not completely characterize this complex.

From a high-spin initial guess wave function, optimized geometries were obtained for two stable solutions: the closed-shell BS(0,0) solution and an open-shell BS(2,2) solution with electronic energy 10.1 kcal/mol below that of BS(0,0). This significant gap indicates that the BS(2,2) solution is likely a closer single-determinant approximation to the electronic structure of this MNIC than the closed-shell solution. The Mulliken spin population on NO (−1.07) in the BS(2,2) solution (Figure 5) is consistent with that observed for triplet

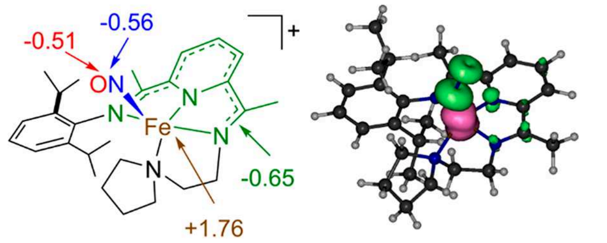

Figure 5. Mulliken spin populations (left) and spin density (right) of MNIC **9**.

NO anion in other FeNO complexes,[71] where the deviation from a formal spin population of −2 arises in part from the metal–ligand covalency, which also reduces the spin population assigned to Fe (1.76). Together with the Mulliken spin populations on PDI (−0.65), this calculation suggests $\{FeNO\}^7$ character with intermediate-spin Fe, a triplet NO^- ligand, and a singly reduced PDI ligand, Fe(III)(↑↑↑)NO^-(↓↓)PDI$^{\bullet-}$(↓). We did not locate any BS solution corresponding to a $\{FeNO\}^6$ complex with a doubly reduced PDI ligand, Fe(III)(↑)$NO^\bullet$(↓)PDI^{2-}(↑↓); however, the calculations presented here cannot rule out the possibility that such a configuration plays a role in the complete description of the complex. The Fe–N–O angle in the BS(2,2)-optimized structure is within the realm typical of NO radical in FeNO complexes at 147.5° (Table 2). This angle is close to the experimentally observed angle of 150.9°. PBE0 predicts a similar Fe–N–O angle for the BS(0,0) structure at 147.3°; in contrast, the ωB97X-D3 functional predicts the NO ligand in the BS(0,0)-optimized structure is bent at 143.3°, intermediate between the angles typically observed for the neutral $NO^\bullet$ radical and NO^-. Given the strong sensitivity of the Fe–N–O angle to the choice of functional for this and other complexes with $\{FeNO\}^7$ character,[81] we turned to molecular orbital analysis for further insight into the electronic structure.

To further probe the electronic character of the ligands and metal in the BS(2,2) configuration, we performed a corresponding orbital (CO) transformation which rotates the orbitals into a basis in which their overlap matrix is diagonal. Employed more generally to compute matrix elements between nonorthogonal spin orbitals,[82,83] the CO transformation is used here to identify COs with $\alpha\beta$ orbital overlaps ($S_{\alpha\beta}$) significantly less than 1. We identified three CO pairs with overlaps significantly less than 1, depicted in the qualitative orbital diagram in Figure 6. The three highest-energy occupied β COs are dominated by Fe d character. In contrast, the highest-energy α CO extends significantly onto the PDI ligand, indicating partial radical character on PDI. The other two α COs with $\alpha\beta$ overlap significantly less than 1 have substantial π^*(NO) character but are also delocalized over the FeNO system, indicating metal–ligand covalent bonding character and reinforcing the redox noninnocence of the NO unit in **9**. The occupation of two COs with π^*(NO) character and a third CO delocalized over the PDI π system supports the assignment of an unusual intermediate-spin Fe(III) coupled to

DOI: 10.1021/jacs.8b08520
J. Am. Chem. Soc. 2018, 140, 17040–17050

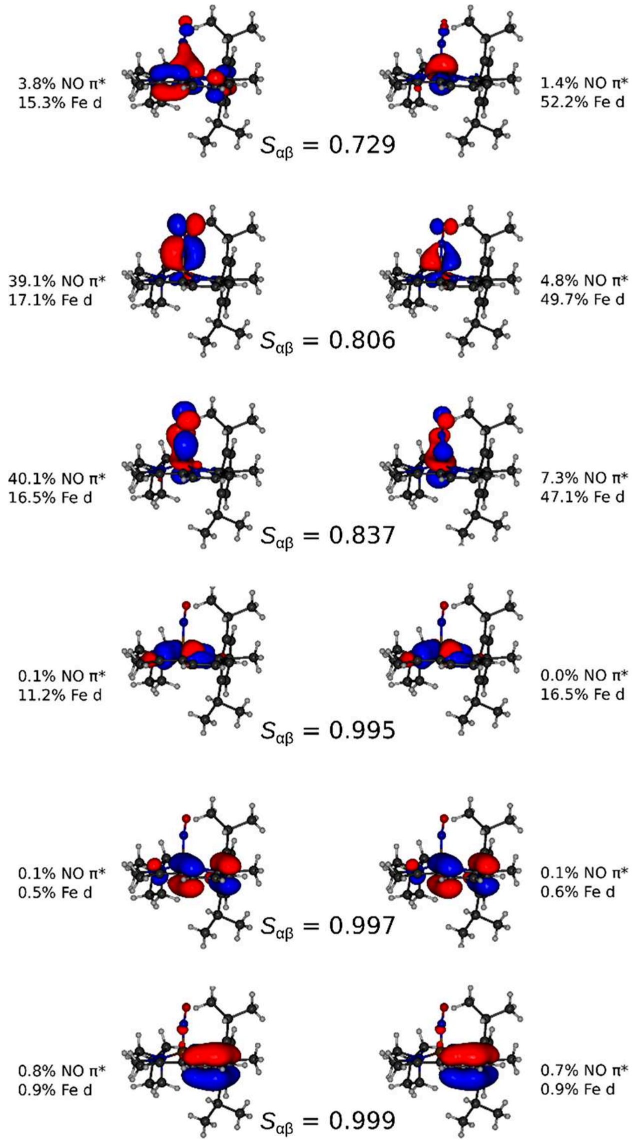

Figure 6. Highest-occupied corresponding orbitals (COs) and $\alpha\beta$ overlaps from the BS(2,2) solution for **9**.

triplet NO^- and a singly reduced PDI ligand. However, the well-documented challenge of accurately predicting spin densities of FeNO complexes with BS-DFT[84] suggests that a multireference treatment would be necessary to confirm this assignment.

Optimized PDI bond lengths for the BS(2,2) solutions of MNIC are summarized in Table 2. The imine C_{imine}−N_{imine} and C_{imine}−C_{ipso} bond lengths from the BS(2,2) optimization are more consistent with experiment, although the distinction from the BS(0,0) solution is small (Table S1). We conclude from the Fe−N−O angle, PDI bond lengths, and BS-DFT calculations that **9** likely possesses $\{FeNO\}^7$ character with an unusual intermediate-spin Fe(III) coupled to triplet NO^- and a singly reduced PDI ligand. Nevertheless, the existence of two BS-DFT solutions with similar energies and different orbital character suggests that a fully multireference electronic structure analysis, which lies beyond the scope of the present work, may be required to fully characterize this complex.

■ CONCLUSION

In conclusion, we have demonstrated that by utilizing the proper sterics and pK_a of pendant base(s) located in the secondary coordination sphere we are able to introduce hemilability into redox-active PDI ligand scaffolds. Through the integration of the triad of redox activity, hemilability, and proton responsivity, into a single ligand scaffold, we have shown that the complexes Fe(^{Pyrr}PDI)$(CO)_2$ (**3**) and Fe(^{Mor}PDI)$(CO)_2$ (**4**) display >40-fold enhancements in the initial rate of NO_2^- reduction. These significant enhancements in the initial rate are facilitated by the hemilability of the pendant base, as illustrated by the isolation of the MNIC intermediates [Fe(^{Pyrr}PDI)(NO)]$^+$ (**9**) and [Fe(^{Mor}PDI)(NO)]$^+$ (**10**). **9** and **10** are unusual examples of nonheme MNICs. The Enemark−Feltham notation that best describes **9** and **10** is somewhat ambiguous: spectroscopic and computational studies suggest that **9** and **10** both have $\{FeNO\}^7$ character, but the noninnocence of both the NO and PDI hints at the possibility that a single electronic configuration may not completely characterize this complex.

■ EXPERIMENTAL SECTION

All reagents were purchased from commercial sources and used as received. The asymmetric ligand [(ArN=C(CH_3))C_2H_3N((CH_3)-C=O)][85] (Ar = 2,6-^{i}Pr-C_6H_3), Fe(^{MeO}PDI)$(CO)_2$ (**7**),[60] and Fe(didpa)$(CO)_2$ (**8**)[48] were synthesized according to literature procedures. [$HNEt_3$][BPh_4] and [HLut][BPh_4] were prepared by adding $NaBPh_4$ in MeOH to an aqueous solution of NEt_3 or lutidine, where the product precipitated as a white solid and was washed with deionized water and dried under high vacuum before use. Solvents were dried and deoxygenated with a Pure-Solv solvent purification system. Deuterated solvents, chloroform-d_1 (D, 99.8%) and methylene chloride-d_2 (D, 99.8%), were purchased from Cambridge Isotope Laboratories, Inc. Carbon monoxide (99.3%) was purchased from Airgas, Inc. Unless otherwise noted, air-sensitive materials were handled and stored on a Schlenk line or in a glovebox under a N_2 atmosphere. Infrared spectra were recorded on a Thermo Scientific Nicolet iS10 FT-IR spectrometer equipped with an ATR accessory. ^{1}H and ^{13}C{^{1}H} NMR spectra were recorded on a Bruker 500 MHz FT-NMR spectrometer. Data are reported in ppm from the solvent resonance as the internal standard unless otherwise noted. UV−vis absorbance data were acquired using a Jasco UV−vis/NIR spectrometer equipped with a Peltier-controlled six-cell linear autosampler. All data were obtained at 298 K in 1 cm quartz cuvettes (Starna Cells). Elemental analyses were performed by ALS Environmental in Tuscon, AZ. Mass spectra were collected using an Agilent GC-MS EI system equipped with an HP-5MS column (30 m × 0.25 mm × 0.25 μm). X-band EPR spectra were recorded on a Bruker EMX spectrometer equipped with an Oxford ESR-900 liquid helium cryostat and a dual-mode microwave cavity. All the samples were prepared in CH_2Cl_2, and perpendicular mode spectra were collected at 11 K with the following parameters: frequency = 9.64 GHz; attenuator = 35.0 dB; modulation frequency = 100.00 kHz; modulation amplitude = 10.02; time constant = 81.92 ms; conversion time = 40.96 ms; number of scans = 4. pK_a values were determined as reported previously.[48] Solution magnetic susceptibilities were calculated from Evan's method NMR measurements.[86] Solid-phase magnetic susceptibilities were recorded on a Johnson Matthey MSB-1 magnetic susceptibility balance that was calibrated with HgCo-$(SCN)_4$. Diamagnetic correction factors were calculated from Pascal's constants.[87]

[(2,6-^{i}Pr-C_6H_3)N=CMe)($C_4H_8NC_2H_4$)N=CMe)C_5H_3N] (^{Pyrr}PDI). In a dry 25 mL pressure vial, [(2,6-^{i}Pr-C_6H_3)N=CMe)(O=CMe)C_5H_3N] (2.02 g, 5.42 mmol) was added with excess 1-(2-aminoethyl)pyrrolidine (3.00 g, 26.3 mmol) and sealed with a pressure lid. The vial was heated in a silicon-based oil bath at 90 °C for 36 h. Methanol was added to the resulting oil to precipitate

DOI: 10.1021/jacs.8b08520
J. Am. Chem. Soc. 2018, 140, 17040−17050

the product, yielding 1.609 g (72%) of a pale yellow powder. FTIR (ATR): 1640 cm^{-1} (C=N). ^1H NMR ($CDCl_3$): δ 8.35 (d, 1H), 8.19 (d, 1H), 7.81 (t, 1H), 7.17−7.08 (m, 3H), 3.74 (t, 2H), 2.93 (t, 2H), 2.75 (m, 2H), 2.65 (m, 4H), 2.45 (s, 3H), 2.24 (s, 3H), 1.82 (m, 4H), 1.15 (dd, 12H). GC-MS (EI) [$M^{\bullet+}$]: m/z calcd for $C_{27}H_{38}N_4$ 418.31 (100.0%), 419.31 (29.2%), 420.32 (2.7%), found 418.300 (100%), 419.300 (30%), 420.300 (3.5%).

Fe(^{Pyrr}PDI)(CO)$_2$ (3). In a multistep synthesis, ^{Pyrr}PDI (0.500 g, 1.20 mmol) was first metalated with $FeBr_2$ (0.270 g, 1.25 mmol) in 10 mL of THF overnight. The solvent was removed in vacuo, and the resulting purple material was redissolved in methanol and filtered through Celite. Et_2O was added to precipitate the product, yielding 0.620 g (82%) of the bluish-purple solid Fe(^{Pyrr}PDI)Br_2(**1**), which was directly used without further purification. FTIR (ATR): 1615, 1580 cm^{-1} (C=N).

Under a N_2 atmosphere, **1** (0.6195 g, 0.9767 mmol), NaHg (1.49 g, 5% Na), and 20 mL of CH_2Cl_2 were added to an 88 mL F−P tube. The tube was sealed with a pressure gauge and charged with 40 psi of CO. The mixture was stirred for 36 h, resulting in a color change from bluish-purple to dark green. The solvent was removed in vacuo. Under N_2, the green material was extracted by Et_2O, and the remaining NaHg mixture was removed by filtration through Celite. The filtered Et_2O solution was left to evaporate overnight to yield dark green crystals of Fe(^{Pyrr}PDI)$(CO)_2$ (**3**) (0.2937 g, 57%). FTIR (ATR): 1942, 1876 cm^{-1} (C=O). ^1H NMR (CD_2Cl_2): δ 8.05 (d, 1H), 8.01 (d, 1H), 7.49 (t, 1H), 7.29−7.20 (m, 3H), 4.37 (m, 2H), 2.85 (m, 2H), 2.68 (s, 3H), 2.59 (br, 4H), 2.47 (m, 2H), 2.32 (s, 3H), 1.75 (br, 4H), 1.22 (d, 6H), 0.99 (d, 6H). $^{13}C\{^1H\}$ NMR (125 MHz, CD_2Cl_2): δ 215.24 (C=O), 156.40 (C_1=N_1), 155.85 (C_2=N_2), 150.19, 146.03, 144.91, 140.71, 126.50, 123.85, 121.25, 120.49, 117.65, 60.46, 58.64, 54.76, 27.67, 24.79, 24.45, 24.01, 16.74, 14.52. ^{57}Fe Mössbauer: δ = −0.089(3) mm s^{-1}; ΔE = 1.197(3) mm s^{-1}. Anal. Calcd for $C_{29}H_{38}FeN_4O_2$: C, 65.66; H, 7.22; N, 10.56. Found: C, 65.44; H, 6.98; N, 10.31.

Fe(^{Mor}PDI)(CO)$_2$ (4). In a multistep synthesis, Fe(^{Mor}PDI)Br_2 (**2**) was first synthesized by dissolving the asymmetric ligand [(ArN=C(CH_3))C_2H_3N((CH_3)C=O] (0.500 g, 1.55 mmol) and $FeBr_2$ (0.334 g, 1.55 mmol) in approximately 40 mL of ethanol into a 100 mL round-bottom Schlenk flask with a stir bar. The solution was heated to 50 °C for 20 min under N_2 gas and stirred. A solution of 4-(2-aminoethyl)morpholine (0.202 g, 1.55 mmol) in 5 mL of ethanol was slowly syringed into the flask, and the solution was left to heat at 78 °C for 12 h under N_2 gas. The solvent was removed in vacuo and a dark blue solid was obtained. Inside the glovebox, the solid was redissolved in 40 mL of CH_2Cl_2 and filtered through Celite. The solvent was again removed in vacuo. The resulting dark blue solid **2** was used in the next step without further purification.

Under a N_2 atmosphere, **2** (0.200 g, 0.308 mmol), NaHg (0.570 g, 5%Na), a stir bar, and approximately 10 mL of CH_2Cl_2 were added to an 88 mL F−P tube. The tube was sealed with a pressure gauge and charged with 40 psi of CO. The mixture was stirred for 36 h, resulting in a color change from bluish-purple to dark green. The solvent was removed in vacuo. Under N_2, the green material was extracted by Et_2O, and the remaining NaHg mixture was removed by filtration through Celite. The filtered Et_2O solution was left to evaporate overnight to yield dark green crystals of Fe(^{Mor}PDI)$(CO)_2$ (**4**) (63%). IR (solid): 1934, 1871 cm^{-1} (C=O). ^1H NMR (500 mHz, CD_2Cl_2): δ 8.08 (d, 1H), 8.04 (d, 1H), 7.52 (t, 1H), 7.25 (m, 3H), 3.69 (t, 4H), 2.80 (t, 2H), 2.71 (s, 3H), 2.57 (s, 4H), 2.50 (sept, 2H), 2.36 (s, 3H), 1.26 (d, 6H), 1.03 (d, 6H). $^{13}C\{^1H\}$ NMR (125 MHz, CD_2Cl_2): δ 214.8 (C=O), 155.9, 155.5, 149.7, 145.5, 144.5, 140.2, 126.1, 123.4, 120.9, 120.1, 117.3, 66.9, 60.9, 58.0, 27.3, 24.4, 24.0, 16.3, 14.2. ^{57}Fe Mössbauer: δ = −0.10(1) mm s^{-1}; ΔE = 1.46(2) mm s^{-1}. Anal. Calcd for $C_{29}H_{38}FeN_4O_3$: C, 63.74; H, 7.01; N, 10.25. Found: C, 63.34; H, 7.09; N, 10.07.

[Fe(^{Pyrr}PDI)(NO)$_2$][BPh$_4$] (5). To a solution of **3** (0.172 g, 0.325 mmol) in THF was added a solution of $NaNO_2$ (0.0454 g, 0.65 mmol) containing a minimal amount of MeOH. The mixture was allowed to equilibrate for about 5 min. While stirring, [$HNEt_3$][BPh_4] (1.3 mmol) was added to the reaction mixture. With continuous stirring, a color change from green to brown was observed within a few hours. The solvents in the brown reaction mixture were removed via vacuum. The crude product was extracted with $CHCl_3$ and filtered through Celite, which was then layered with Et_2O to yield brown **5** (204 mg, 74%). Vapor diffusion of Et_2O into $CHCl_3$ solutions of **5** resulted in fine needles for X-ray analysis. The ^{15}NO analogue was synthesized as described above utilizing $Na^{15}NO_2$ in place of $NaNO_2$. FTIR (ATR): 1785/1716, 1752/1682 cm^{-1} (^{14}N=O/^{15}N=O); 732, 702 cm^{-1} (BPh_4). ^{57}Fe Mössbauer: δ = 0.032(3) mm s^{-1}; ΔE = 0.82(9) mm s^{-1}. EPR (X-band, CH_2Cl_2, 11 K): g = 2.01. Anal. Calcd for $C_{51}H_{58}BFeN_6O_2$: C, 71.75; H, 6.85; N, 9.84. Found: C, 71.56; H, 6.84; N, 8.99.

[Fe(^{Pyrr}PDI)(NO)$_2$][BPh$_4$] (6). The procedure described above for synthesis of the DNIC **5** was followed, replacing **4** with **3** (32% yield). FTIR (ATR): 1783/1749, 1709/1677 cm^{-1} (^{14}N=O/^{15}N=O); 734, 705 cm^{-1} (BPh_4). EPR (X-band, CH_2Cl_2, 11 K): g = 2.01. Anal. Calcd for $C_{51}H_{58}BFeN_6O_3$: C, 70.43; H, 6.72; N, 9.66. Found: C, 69.97; H, 6.92; N, 9.48.

[Fe(^{Pyrr}PDI)(NO)][BPh$_4$] (9). To a suspension of **3** (0.158 g, 0.297 mmol) in THF/MeOH (approximately 1:4 by volume) was added a MeOH solution of $NaNO_2$ (2.46 mL, 0.297 mmol). The mixture was allowed to equilibrate for about 5 min. While stirring, [HEt_3N][BPh_4] (0.50 g, 1.2 mmol) was added to the reaction mixture, which shortly led to the disappearance of the dark green color and eventually the formation of a blue precipitate. The solvent was then decanted into a Celite filter to isolate the precipitate, followed by treating the dried Celite mixture with CH_2Cl_2 to redissolve the blue product. After filtering through a fresh Celite plug, the blue CH_2Cl_2 solution was layered with an equal volume of Et_2O and left undisturbed for 3 days to afford blue crystals of [Fe(^{Pyrr}PDI)(NO)][BPh_4] (**9**) that were suitable for X-ray diffraction (0.1728 g, 71%). The ^{15}NO analogue was synthesized as described above utilizing $Na^{15}NO_2$ in place of $NaNO_2$. FTIR (ATR): 1666/1635 cm^{-1} (^{14}N=O/^{15}N=O); 729, 702 cm^{-1} (BPh_4). ^1H NMR (500 MHz, CD_2Cl_2, δ): 7.80 (d, 1H), 7.79 (d, 1H), 7.69 (t, 1H), 7.40−7.26 (m, 3H), 7.31 (br, 8H), 6.99 (t, 8H), 6.83 (t, 4H), 3.45−3.32 (m, 2H), 2.91 (dd, 1H), 2.84−2.81 (m, 2H), 2.55−2.46 (m, 2H), 2.42 (s, 3H), 2.39 (s, 3H), 2.13 (dd, 1H), 1.86−1.71 (m, 2H), 1.60 (br, 1H), 1.43 (d, 3H), 1.38 (br, 1H), 1.18 (d, 3H), 1.12 (d, 3H), 0.91 (d, 3H). $^{13}C\{^1H\}$ NMR (125 MHz, CD_2Cl_2): δ 170.99, 165.03, 164.64, 164.25, 163.86, 163.00, 153.21, 152.60, 143.23, 141.19, 139.87, 136.33, 128.76, 126.79, 126.31, 126.02, 125.79, 125.13, 124.80, 122.14, 63.03, 60.27, 51.50, 29.21, 27.83, 25.76, 24.75, 24.67, 22.99, 22.61, 22.17, 18.72, 15.56. ^{57}Fe Mössbauer: δ = 0.094(3) mm s^{-1}; ΔE = 0.489(5) mm s^{-1}. Anal. Calcd for $C_{51}H_{58}BFeN_5O$: C, 74.37; H, 7.10; N, 8.50. Found: C, 73.92; H, 6.96; N, 8.40.

[Fe(^{Mor}PDI)(NO)][BPh$_4$] (10). The procedure described above for synthesis of the MNIC **9** was followed, replacing **4** with **3**. The blue-green crystalline solid of **10** was isolated (0.0759 g, 35%). Crystals suitable for X-ray diffraction were grown by vapor diffusion of Et_2O into a THF solution of **10**. The ^{15}NO analogue was synthesized as described above utilizing $Na^{15}NO_2$ in place of $NaNO_2$. FTIR (ATR): 1686/1654 cm^{-1} (^{14}N=O/^{15}N=O); 734, 705 cm^{-1} (BPh_4). ^1H NMR (500 MHz, CD_2Cl_2): δ 7.82 (t, 2H), 7.72 (t, 1H), 7.46−7.37 (m, 3H), 7.31 (br, 8H), 6.99 (t, 8H), 6.83 (t, 4H), 3.68 (q, 2H), 3.64−3.60 (m, 1H), 3.42−3.25 (m, 2H), 3.33 (dd, 1H), 3.21 (dd, 1H), 3.08 (td, 1H), 2.78 (d, 1H), 2.57 (d, 1H), 2.57−2.46 (m, 2H), 2.41 (s, 3H), 2.40 (s, 3H), 2.34 (dd, 2H), 1.55 (br, 2H), 1.40 (d, 3H), 1.32 (d, 3H), 1.13 (d, 3H), 0.99 (d, 3H). $^{13}C\{^1H\}$ NMR (125 MHz, CD_2Cl_2): δ 171.65, 165.07, 164.68, 164.28, 163.89, 163.48, 153.12, 152.73, 143.15, 141.42, 139.92, 136.35, 129.04, 126.98, 126.53, 126.07, 125.93, 125.28, 122.18, 61.26, 60.43, 59.63, 50.42, 29.27, 27.81, 25.84, 24.92, 24.79, 22.97, 18.83, 15.69. ^{57}Fe Mössbauer: δ = 0.095(5) mm s^{-1}; ΔE = 0.415(9) mm s^{-1}. Anal. Calcd for $C_{51}H_{58}BFeN_5O_2$: C, 72.95; H, 6.96; N, 8.34. Found: C, 72.95; H, 6.93; N, 8.24.

Mössbauer Spectra. Mössbauer spectra were recorded at room temperature with a constant acceleration spectrometer (Wissel GMBH, Germany) in a horizontal transmission mode using a 50 mCi ^{57}Co source. Approximately 0.200 g of sample was crushed in a

DOI: 10.1021/jacs.8b08520
J. Am. Chem. Soc. 2018, 140, 17040−17050

Mössbauer sample holder, and a drop of Paratone-N was used to cover the sample to prevent oxidation. Data acquisition varied from 2 days to 7 days to get a statistically reasonable spectrum for each sample to analyze. The velocity scale was normalized with respect to metallic iron at room temperature; hence all isomer shifts were recorded relative to metallic iron. The Mössbauer spectra were fitted by assuming Lorentzian line shapes using the NORMOS (Wissel GMBH) least-squares fitting program. The isomer shifts and quadrupole splitting parameters were determined from the fitted spectra.

UV−Vis Kinetics. All samples were prepared under an N_2 atmosphere inside a glovebox. A typical kinetics experiment was performed by preparing an acetonitrile solution consisting of 225 μM **3** and 550 μM tetrabutylammonium nitrite. A 3.0 mL amount of this solution was added to a quartz cuvette equipped with a stir bar and sealed with a pierceable septum. Into a syringe equipped with a needle, an excess of either a 9 mM [$HNEt_3$][BPh_4] or a 9 mM [HLut][BPh_4] solution was drawn, and the needle was pierced into a scintillation vial equipped with a septum to keep the solution under an N_2 atmosphere. The cuvette and syringe were brought outside of the box where the cuvette was placed into the spectrometer to equilibrate at 25 °C for 10 min before injection of 0.3 mL of the acid solution into the cuvette while starting the spectrometer.

Computational Methods. The electronic structures were studied through BS-DFT calculations. This approach breaks spin-symmetry in the initial guess wave function to converge an electronic state with quasi-localized spins on different sites in the complex.[88] The resulting spin density is unphysically asymmetric, but the procedure yields a qualitatively correct total electron density and energy for an antiferromagnetically coupled electronic ground state within a single-determinant KS-DFT framework.[89] We adopt the notation BS(m,n) to represent a broken-symmetry solution with m unpaired electrons on Fe antiferromagnetically coupled to n unpaired electrons on the ligands. The unpaired spin-down electron density was not forced to localize on the PDI or NO ligand specifically. Following the DFT functional benchmarking procedure described in the Supporting Information, the BP86 functional was selected for analysis of **5**, while the hybrid PBE0 functional was selected for the final electronic structure analysis of **9**. All reported BS-DFT single-point energy evaluations, geometry optimizations, and Mulliken charge/spin analyses were performed with the functionals indicated above and the def2-TZVP(-f) basis set with the RIJCOSX approximation[90] in ORCA 4.0.1.2.[91]

X-ray Crystallography. Single-crystal X-ray diffraction data for **3** and **10** were collected on a Rigaku Oxford Diffraction XtaLABPRO X-ray diffractometer equipped with a Pilatus P200 K hybrid photon counting detector. Reflections were collected at 100(2) K using graphite-monochromated Mo $K_{\alpha1}$ radiation using a data collection strategy calculated within CrystalClear to ensure maximum data redundancy and percent completeness.[92] Data processing, including frame integration, Lorentz−polarization corrections, and final cell parameter calculations, was completed using CrysAlisPro.[93] A multiscan absorption correction was applied using the SCALE3 ABSPACK scaling algorithm integrated into CrysAlisPro.[94] The crystal structure was solved via intrinsic phasing using ShelXT and refined with least-squares minimization with ShelXL in the Olex2 graphical user interface.[95−97] The space group was unambiguously verified by PLATON.[98] The final structural refinement included anisotropic temperature factors on all non-hydrogen atoms, and hydrogen atoms were attached via the riding model at calculated positions using appropriate HFIX commands.

Diffraction intensities for **4**, **5**, **9**, and **6** were collected at 150 (**4**) and 173 K on a Bruker Apex2 DUO CCD diffractometer using Mo K_α (**4**) and Cu K_α radiation, λ = 0.710 73 and 1.541 78 Å, respectively. Absorption corrections were applied by SADABS.[99] Space groups were determined based on systematic absences (**4**) and intensity statistics (**5**, **9**, **6**). Structures were solved by direct methods and Fourier techniques and refined on F^2 using full matrix least-squares procedures. All non-H atoms were refined with anisotropic thermal parameters. H atoms in **5**, **9**, and **6** were refined in calculated positions in a rigid group model. Positions of H atoms in **4** were found on the residual density map and refined with isotropic thermal parameters. All calculations were performed by the Bruker SHELXL-2014/7 package.[96]

■ ASSOCIATED CONTENT

Supporting Information

The Supporting Information is available free of charge on the ACS Publications website at DOI: 10.1021/jacs.8b08520.

Spectroscopic, kinetic, and computational data (PDF)
X-ray crystallographic data (CIF)

■ AUTHOR INFORMATION

Corresponding Authors

*tim.kowalczyk@wwu.edu
*john.gilbertson@wwu.edu

ORCID

Tim Kowalczyk: 0000-0003-1806-059X
John D. Gilbertson: 0000-0003-2450-0846

Notes

The authors declare no competing financial interest.

■ ACKNOWLEDGMENTS

This research was supported by an award from the National Institutes of Health (R15GM123380 to J.D.G.) and NSF MRI awards (CHE-1429164 and CHE-1532269). M.Y.D. and T.K. acknowledge support from NSF award CHE-1664674. We thank Eric Reinheimer (Rigaku) for assistance with crystallography and an anonymous reviewer for valuable feedback on the electronic structure analysis.

■ REFERENCES

(1) Hill, B. G.; Dranka, B. P.; Bailey, S. M.; Lancaster, J. R., Jr.; Darley-Usmar, V. M. What Part of NO Don't You Understand? Some Answers to the Cardinal Questions in Nitric Oxide Biology. *J. Biol. Chem.* **2010**, *285*, 19699−19704.

(2) Cosby, K.; Partovi, K. S.; Crawford, J. H.; Patel, R. P.; Reiter, C. D.; Martyr, S.; Yang, B. K.; Waclawiw, M. A.; Zalos, G.; Xu, X.; Huang, K. T.; Shields, H.; Kim-Shapiro, D. B.; Schechter, A. N.; Cannon, R. O., III; Gladwin, M. T. Nitrite reduction to nitric oxide by deoxyhemoglobin vasodilates the human circulation. *Nat. Med.* **2003**, *9*, 1498−1505.

(3) Maia, L. B.; Moura, J. J. G. How Biology Handles Nitrite. *Chem. Rev.* **2014**, *114*, 5273−5357.

(4) Fields, S. Global Nitrogen: Cycling out of Control. *Environ. Health Perspect.* **2004**, *112*, A556−A563.

(5) Grant, S. B.; Saphores, J.-D.; Feldman, D. L.; Hamilton, A. J.; Fletcher, T. D.; Cook, P. L. M.; Stewardson, M.; Sanders, B. F.; Levin, L. A.; Ambrose, R. F.; Deletic, A.; Brown, R.; Jiang, S. C.; Rosso, D.; Cooper, W. J.; Marusic, I. Taking the "Waste" Out of "Wastewater" for Human Water Security and Ecosystem Sustainability. *Science* **2012**, *337*, 681−686.

(6) Ward, M. H.; deKok, T. M.; Levallois, P.; Brender, J.; Gulis, G.; Nolan, B. T.; VanDerslice, J. Workgroup Report: Drinking-Water Nitrate and Health—Recent Findings and Research Needs. *Environ. Health Perspect.* **2005**, *113*, 1607−1614.

(7) Hardison, R. C. A brief history of hemoglobins: plant, animal, protist, and bacteria. *Proc. Natl. Acad. Sci. U. S. A.* **1996**, *93*, 5675−5679.

(8) Gladwin, M. T.; Kim-Shapiro, D. B. The functional nitrite reductase activity of the heme-globins. *Blood* **2008**, *112*, 2636−2647.

(9) Shiva, S.; Huang, Z.; Grubina, R.; Sun, J.; Ringwood, L. A.; MacArthur, P. H.; Xu, X.; Murphy, E.; Darley-Usmar, V. M.; Gladwin, M. T. Deoxymyoglobin is a nitrite reductase that generates nitric

DOI: 10.1021/jacs.8b08520
J. Am. Chem. Soc. 2018, 140, 17040−17050

oxide and regulates mitochondrial respiration. *Circ. Res.* **2007**, *100*, 654−661.
(10) Cossins, A. R.; Williams, D. R.; Foulkes, N. S.; Berenbrink, M.; Kipar, A. Diverse cell-specific expression of myoglobin isoforms in brain, kidney, gill and liver of the hypoxia-tolerant carp and zebrafish. *J. Exp. Biol.* **2009**, *212*, 627−638.
(11) Omar, S. A.; Webb, A. J. Nitrite reduction and cardiovascular protection. *J. Mol. Cell. Cardiol.* **2014**, *73*, 57−69.
(12) Heinecke, J.; Ford, P. C. Mechanistic studies of nitrite reactions with metalloproteins and models relevant to mammalian physiology. *Coord. Chem. Rev.* **2010**, *254*, 235−247.
(13) Williams, P. A.; Fülöp, V.; Garman, E. F.; Saunders, N. F.; Ferguson, S. J.; Hajdu, J. Haem-ligand switching during catalysis in crystals of a nitrogen-cycle enzyme. *Nature* **1997**, *389*, 406−412.
(14) Ranghino, G.; Scorza, E.; Sjögren, T.; Williams, P. A.; Ricci, M.; Hajdu, J. Quantum Mechanical Interpretation of Nitrite Reduction by Cytochrome cd1 Nitrite Reductase from Paracoccus pantotrophus. *Biochemistry* **2000**, *39*, 10958−10966.
(15) Huang, K. T.; Keszler, A.; Patel, N.; Patel, R. P.; Gladwin, M. T.; Kim-Shapiro, D. B.; Hogg, N. The Reaction between Nitrite and Deoxyhemoglobin reassessment of reaction kinetics and stoichiometry. *J. Biol. Chem.* **2005**, *280*, 31126−31131.
(16) Perissinotti, L. L.; Marti, M. A.; Doctorovich, F.; Luque, F. J.; Estrin, D. A. A Microscopic Study of the Deoxyhemoglobin-Catalyzed Generation of Nitric Oxide from Nitrite Anion. *Biochemistry* **2008**, *47*, 9793−9802.
(17) Silaghi-Dumitrescu, R. Linkage Isomerism in Nitrite Reduction by Cytochrome cd1 Nitrite Reductase. *Inorg. Chem.* **2004**, *43*, 3715−3718.
(18) Proton-Coupled Electron Transfer Themed Issue. *Chem. Rev.* **2010**, *110*, 6937−7100.
(19) Dempsey, J. L.; Winkler, J. R.; Gray, H. B. Proton-Coupled Electron Flow in Protein Redox Machines. *Chem. Rev.* **2010**, *110*, 7024−7039.
(20) Warren, J. J.; Mayer, J. M. Moving Protons and Electrons in Biomimetic Systems. *Biochemistry* **2015**, *54*, 1863−1878.
(21) Chirik, P. J. Preface: Forum on Redox-Active Ligands. *Inorg. Chem.* **2011**, *50*, 9737−9740.
(22) Berben, L. A.; de Bruin, B.; Heyduk, A. F. Non-Innocent Ligands. *Chem. Commun.* **2015**, *51*, 1553−1554.
(23) Jeffrey, J. C.; Rauchfuss, T. B. Metal complexes of hemilabile ligands. Reactivity and structure of dichlorobis(o-(diphenylphosphino)anisole)ruthenium(II). *Inorg. Chem.* **1979**, *18*, 2658−2666.
(24) Bassetti, M. Kinetic Evaluation of Ligand Hemilability in Transition Metal Complexes. *Eur. J. Inorg. Chem.* **2006**, *2006*, 4473−4482.
(25) Annibale, V. T.; Song, D. Multidentate actor ligands as versatile platforms for small molecule activation and catalysis. *RSC Adv.* **2013**, *3*, 11432−11449.
(26) Braunstein, P.; Naud, F. Hemilability of Hybrid Ligands and the Coordination Chemistry of Oxazoline-Based Systems. *Angew. Chem., Int. Ed.* **2001**, *40*, 680−699.
(27) Weng, Z.; Teo, S.; Hor, T. S. A. Metal Unsaturation and Ligand Hemilability in Suzuki Coupling. *Acc. Chem. Res.* **2007**, *40*, 676−684.
(28) Borovik, A. S. Bioinspired Hydrogen Bond Motifs in Ligand Design: The Role of Noncovalent Interactions in Metal Ion Mediated Activation of Dioxygen. *Acc. Chem. Res.* **2005**, *38*, 54−61.
(29) Helm, M. L.; Stewart, M. P.; Bullock, R. M.; DuBois, M. R.; DuBois, D. L. A synthetic nickel electrocatalyst with a turnover frequency above 100,000 s^{-1} for H_2 production. *Science* **2011**, *333*, 863−866.
(30) Nieto, I.; Livings, M. S.; Sacci, J. B.; Reuther, L. E.; Zeller, M.; Papish, E. T. Transfer Hydrogenation in Water via a Ruthenium Catalyst with OH Groups near the Metal Center on a bipy Scaffold. *Organometallics* **2011**, *30*, 6339−6342.
(31) Costentin, C.; Drouet, S.; Robert, M.; Saveant, J.-M. A local proton source enhances CO2 electroreduction to CO by a molecular Fe catalyst. *Science* **2012**, *338*, 90−94.
(32) O'Hagan, M.; Ho, M.-H.; Yang, J. Y.; Appel, A. M.; DuBois, M. R.; Raugei, S.; Shaw, W. J.; DuBois, D. L.; Bullock, R. M. Proton Delivery and Removal in [Ni(PR2NR′2)2]2+ Hydrogen Production and Oxidation Catalysts. *J. Am. Chem. Soc.* **2012**, *134*, 19409−19424.
(33) Geri, J. B.; Szymczak, N. K. A Proton-Switchable Bifunctional Ruthenium Complex That Catalyzes Nitrile Hydroboration. *J. Am. Chem. Soc.* **2015**, *137*, 12808−12814.
(34) Rigsby, M. L.; Wasylenko, D. J.; Pegis, M. L.; Mayer, J. M. Medium Effects Are as Important as Catalyst Design for Selectivity in Electrocatalytic Oxygen Reduction by Iron−Porphyrin Complexes. *J. Am. Chem. Soc.* **2015**, *137*, 4296−4299.
(35) Loewen, N. D.; Thompson, E. J.; Kagan, M.; Banales, C. L.; Myers, T. W.; Fettinger, J. C.; Berben, L. A. A pendant proton shuttle on [Fe4N(CO)12]− alters product selectivity in formate vs. H2 production via the hydride [H−Fe4N(CO)12]−. *Chem. Sci.* **2016**, *7*, 2728−2735.
(36) Ford, C. L.; Park, Y. J.; Matson, E. M.; Gordon, Z.; Fout, A. R. *Science* **2016**, *354*, 741−743.
(37) Chapovetsky, A.; Do, T. H.; Haiges, R.; Takase, M. K.; Marinescu, S. C. Proton-Assisted Reduction of CO2 by Cobalt Aminopyridine Macrocycles. *J. Am. Chem. Soc.* **2016**, *138*, 5765−5768.
(38) Roy, S.; Sharma, B.; Pecaut, J.; Simon, P.; Fontecave, M.; Tran, P. D.; Derat, E.; Artero, V. Molecular Cobalt Complexes with Pendant Amines for Selective Electrocatalytic Reduction of Carbon Dioxide to Formic Acid. *J. Am. Chem. Soc.* **2017**, *139*, 3685−3696.
(39) Cioncoloni, G.; Roger, I.; Wheatley, P. S.; Wilson, C.; Morris, R. E.; Sproules, S.; Symes, M. D. Proton-Coupled Electron Transfer Enhances the Electrocatalytic Reduction of Nitrite to NO in a Bioinspired Copper Complex. *ACS Catal.* **2018**, *8*, 5070−5084.
(40) Morrow, T. J.; Christman, W. E.; Williams, J. Z.; Arulsamy, N.; Goroncya, A.; Hulley, E. B. Ligand dynamics and protonation preferences of Rh and Ir complexes bearing an almost, but not quite, pendent base. *Dalton Trans.* **2018**, *47*, 2670−2682.
(41) Chaudhuri, P.; Hess, M.; Müller, J.; Hildenbrand, K.; Bill, E.; Weyhermüller, T.; Wieghardt, K. Aerobic Oxidation of Primary Alcohols (Including Methanol) by Copper(II)− and Zinc(II)−Phenoxyl Radical Catalysts. *J. Am. Chem. Soc.* **1999**, *121*, 9599−9610.
(42) Hubner, R.; Weber, S.; Strobel, S.; Sarkar, B.; Zalis, S.; Kaim, W. Reversible Intramolecular Single-Electron Oxidative Addition Involving a Hemilabile Noninnocent Ligand. *Organometallics* **2011**, *30*, 1414−1418.
(43) Thompson, E. J.; Berben, L. A. Electrocatalytic Hydrogen Production by an Aluminum(III) Complex: Ligand-Based Proton and Electron Transfer. *Angew. Chem., Int. Ed.* **2015**, *54*, 11642−11646.
(44) Horak, K. T.; Agapie, T. Dioxygen Reduction by a Pd(0)−Hydroquinone Diphosphine Complex. *J. Am. Chem. Soc.* **2016**, *138*, 3443−3452.
(45) Henthorn, J. T.; Agapie, T. Modulation of Proton-Coupled Electron Transfer through Molybdenum−Quinonoid Interactions. *Inorg. Chem.* **2016**, *55*, 5337−5342.
(46) Chang, M.-C.; McNeece, A. J.; Hill, E. A.; Filatov, A. S.; Anderson, J. S. Ligand-Based Storage of Protons and Electrons in Dihydrazonopyrrole Complexes of Nickel. *Chem. - Eur. J.* **2018**, *24*, 8001−8008.
(47) Rosenkoetter, K. E.; Wojnar, M. K.; Charette, B. J.; Ziller, J. W.; Heyduk, A. F. Hydrogen-Atom Noninnocence of a Tridentate [SNS] Pincer Ligand. *Inorg. Chem.* **2018**, *57*, 9728−9737.
(48) Delgado, M.; Sommer, S. K.; Swanson, S. P.; Berger, R. F.; Seda, T.; Zakharov, L. N.; Gilbertson, J. D. Probing the Protonation State and the Redox-Active Sites of Pendant Base Iron(II) and Zinc(II) Pyridinediimine Complexes. *Inorg. Chem.* **2015**, *54*, 7239−7248.
(49) Kwon, Y.; Delgado, M.; Zakharov, L.; Seda, T.; Gilbertson, J. D. Nitrite reduction by a pyridinediimine complex with a proton-responsive secondary coordination sphere. *Chem. Commun.* **2016**, *52*, 11016−11019.

DOI: 10.1021/jacs.8b08520
J. Am. Chem. Soc. 2018, 140, 17040−17050

(50) Delgado, M.; Gilbertson, J. D. Ligand-based reduction of nitrate to nitric oxide utilizing a proton-responsive secondary coordination sphere. *Chem. Commun.* **2017**, *53*, 11249−11252.
(51) Grützmacher, H. Cooperating ligands in catalysis. *Angew. Chem., Int. Ed.* **2008**, *47*, 1814−1818.
(52) van der Vlugt, J. I. Cooperative Catalysis with First-Row Late Transition Metals. *Eur. J. Inorg. Chem.* **2012**, *2012*, 363−375.
(53) Askevold, B.; Roesky, H. W.; Schneider, S. Learning from the Neighbors: Improving Homogeneous Catalysts with Functional Ligands Motivated by Heterogeneous and Biocatalysis. *ChemCatChem* **2012**, *4*, 307−320.
(54) Kaljurand, I.; Kütt, A.; Sooväli, L.; Rodima, T.; Mäemets, V.; Leito, I.; Koppel, I. A. Extension of the Self-Consistent Spectrophotometric Basicity Scale in Acetonitrile to a Full Span of 28 pKa Units: Unification of Different Basicity Scales. *J. Org. Chem.* **2005**, *70*, 1019−1028.
(55) Coetzee, J. F.; Padmanabhan, G. R. Properties of Bases in Acetonitrile as Solvent. IV. Proton Acceptor Power and Homoconjugation of Mono- and Diamines. *J. Am. Chem. Soc.* **1965**, *87*, 5005−5010.
(56) A τ value 1 corresponds to an ideal trigonal bipyramidal geometry, whereas a τ value of 0 corresponds to an ideal square pyramidal geometry. See: Addison, A. W.; Rao, T. N.; Reedjik, J.; van Rijn, J.; Verschoor, G. C. Synthesis, structure, and spectroscopic properties of copper(II) compounds containing nitrogen−sulphur donor ligands; the crystal and molecular structure of aqua[1,7-bis(N-methylbenzimidazol-2′-yl)-2,6-dithiaheptane]copper(II) perchlorate. *J. Chem. Soc., Dalton Trans.* **1984**, 1349.
(57) Martin, R. L.; Taylor, D. Bending of linear nitric oxide ligands in four-coordinate transition metal complexes. Crystal and molecular structure of dinitrosyldithioacetylacetonatocobalt(-I), Co(NO)2-(SacSac). *Inorg. Chem.* **1976**, *15*, 2970−2976.
(58) Enemark, J. H.; Feltham, R. D. Principles of structure, bonding, and reactivity for metal nitrosyl complexes. *Coord. Chem. Rev.* **1974**, *13*, 339−406.
(59) Speelman, A. L.; Zhang, B.; Silakov, A.; Skodje, K. M.; Alp, E. E.; Zhao, J.; Hu, M. Y.; Kim, E.; Krebs, C.; Lehnert, N. Unusual Synthetic Pathway for an {Fe(NO)2}9 Dinitrosyl Iron Complex (DNIC) and Insight into DNIC Electronic Structure via Nuclear Resonance Vibrational Spectroscopy. *Inorg. Chem.* **2016**, *55*, 5485−5501.
(60) Given the unknown mechanism of NO formation and the potential presence of competitive reactions, the initial rate method was employed. See: Casado, J.; Lopez-Quintela, M. A.; Lorenzo-Barral, F. M. The initial rate method in chemical kinetics: Evaluation and experimental illustration. *J. Chem. Educ.* **1986**, *63*, 450−452.
(61) Thammavongsy, Z.; Seda, T.; Zakharov, L. N.; Kaminsky, W.; Gilbertson, J. D. Ligand-Based Reduction of CO2 and Release of CO on Iron(II). *Inorg. Chem.* **2012**, *51*, 9168−9170.
(62) Burns, K. T.; Marks, W. R.; Cheung, P. M.; Seda, T.; Zakharov, L. N.; Gilbertson, J. D. Uncoupled Redox-Inactive Lewis Acids in the Secondary Coordination Sphere Entice Ligand-Based Nitrite Reduction. *Inorg. Chem.* **2018**, *57*, 9601−9610.
(63) Kupper, C.; Rees, J. A.; Dechert, S.; DeBeer, S.; Meyer, F. Complete Series of {FeNO}8, {FeNO}7, and {FeNO}6 Complexes Stabilized by a Tetracarbene Macrocycle. *J. Am. Chem. Soc.* **2016**, *138*, 7888−7898.
(64) Serres, R. G.; Grapperhaus, C. A.; Bothe, E.; Bill, E.; Weyhermuller, T.; Neese, F.; Wieghardt, K. Structural, Spectroscopic, and Computational Study of an Octahedral, Non-Heme {Fe−NO}6−8 Series: [Fe(NO)(cyclam-ac)]2+/+/0. *J. Am. Chem. Soc.* **2004**, *126*, 5138−5153.
(65) Wyllie, G. R. A.; Scheidt, W. R. Solid-State Structures of Metalloporphyrin NOx Compounds. *Chem. Rev.* **2002**, *102*, 1067−1090.
(66) Roncaroli, F.; Videla, M.; Slep, L. D.; Olabe, J. A. New features in the redox coordination chemistry of metal nitrosyls {M−NO+; M−NO; M−NO−(HNO)}. *Coord. Chem. Rev.* **2007**, *251*, 1903−1930.
(67) Richter-Addo, G. B.; Wheeler, R. A.; Hixson, C. A.; Chen, L.; Khan, M. A.; Ellison, M. K.; Schulz, C. E.; Scheidt, W. R. Unexpected Nitrosyl-Group Bending in Six-Coordinate {M(NO)}6 σ-Bonded Aryl(iron) and -(ruthenium) Porphyrins. *J. Am. Chem. Soc.* **2001**, *123*, 6314−6326.
(68) Roberts, S. A.; Weichsel, A.; Qiu, Y.; Shelnutt, J. A.; Walker, F. A.; Montfort, W. R. Ligand-Induced Heme Ruffling and Bent NO Geometry in Ultra-High-Resolution Structures of Nitrophorin 4. *Biochemistry* **2001**, *40*, 11327−11337.
(69) Linder, D. P.; Rodgers, K. R.; Banister, J.; Wyllie, G. R. A.; Ellison, M. K.; Scheidt, W. R. Five-Coordinate FeIIINO and FeIICO Porphyrinates: Where Are the Electrons and Why Does It Matter? *J. Am. Chem. Soc.* **2004**, *126*, 14136−14148.
(70) Lanucara, F.; Chiavarino, B.; Crestoni, M. E.; Scuderi, D.; Sinha, R. K.; Maitre, P.; Fornarini, S. Naked Five-Coordinate FeIII(NO) Porphyrin Complexes: Vibrational and Reactivity Features. *Inorg. Chem.* **2011**, *50*, 4445−4452.
(71) Speelman, A. L.; Zhang, B.; Krebs, C.; Lehnert, N. Structural and Spectroscopic Characterization of a High-Spin {FeNO}6 Complex with an Iron(IV)−NO− Electronic Structure. *Angew. Chem., Int. Ed.* **2016**, *55*, 6685−6688.
(72) Hong, S.; Yan, J. J.; Karmalkar, D. G.; Sutherlin, K. D.; Kim, J.; Lee, Y.-M.; Goo, Y.; Mascharak, P. K.; Hedman, B.; Hodgson, K. O.; Karlin, K. D.; Solomon, E. I.; Nam, W. A mononuclear nonheme {FeNO}6 complex: synthesis and structural and spectroscopic characterization. *Chem. Sci.* **2018**, *9*, 6952−6960.
(73) McCleverty, J. A. Chemistry of Nitric Oxide Relevant to Biology. *Chem. Rev.* **2004**, *104*, 403−418.
(74) Bart, S. C.; Chlopek, K.; Bill, E.; Bouwkamp, M. W.; Lobkovsky, E.; Neese, F.; Wieghardt, K.; Chirik, P. J. Electronic Structure of Bis(imino)pyridine Iron Dichloride, Monochloride, and Neutral Ligand Complexes: A Combined Structural, Spectroscopic, and Computational Study. *J. Am. Chem. Soc.* **2006**, *128*, 13901−13912.
(75) Tondreau, A. M.; Milsmann, C.; Lobkovsky, E.; Chirik, P. J. Oxidation and Reduction of Bis(imino)pyridine Iron Dicarbonyl Complexes. *Inorg. Chem.* **2011**, *50*, 9888−9895.
(76) Given the resonance hybrid between Fe(II)PDI^{2-} and Fe(0) PDI^0 in **3**, one could also envisage the electronic structure of Fe(I) PDI^0 being valid to describe the electronic structure in **9**. Our corresponding orbital analysis suggests contributions from both $\{FeNO\}^6$ and $\{FeNO\}^8$ configurations. Regardless, the isomer shift in **9** suggests the iron center is more oxidized than in **5**.
(77) The electronic structure of $\{Fe(NO)_2\}^9$ DNICs can also be qualitatively described as a resonance hybrid of $\{Fe^{II}(^{\bullet}NO)(NO^-)\}^9$ and $\{Fe^{III}(NO^-)_2\}^9$ electronic states. See: Tsai, M.-L.; Tsou, C.-C.; Liaw, W.-F. Dinitrosyl Iron Complexes (DNICs): From Biomimetic Synthesis and Spectroscopic Characterization toward Unveiling the Biological and Catalytic Roles of DNICs. *Acc. Chem. Res.* **2015**, *48*, 1184−1193.
(78) Ye, S.; Neese, F. The Unusual Electronic Structure of Dinitrosyl Iron Complexes. *J. Am. Chem. Soc.* **2010**, *132*, 3646−3647.
(79) Pulukkody, R.; Darensbourg, M. Y. Synthetic Advances Inspired by the Bioactive Dinitrosyl Iron Unit. *Acc. Chem. Res.* **2015**, *48*, 2049−2058.
(80) Ortuño, M. A.; Cramer, C. J. Multireference Electronic Structures of Fe−Pyridine(diimine) Complexes over Multiple Oxidation States. *J. Phys. Chem. A* **2017**, *121*, 5932−5939.
(81) Berto, T. C.; Speelman, A. L.; Zheng, S.; Lehnert, N. Mono- and dinuclear non-heme iron−nitrosyl complexes: Models for key intermediates in bacterial nitric oxide reductases. *Coord. Chem. Rev.* **2013**, *257*, 244−259.
(82) Yost, S. R.; Kowalczyk, T.; Van Voorhis, T. A multireference perturbation method using non-orthogonal Hartree-Fock determinants for ground and excited states. *J. Chem. Phys.* **2013**, *139*, 174104.
(83) King, H. F. Corresponding Orbitals and the Nonorthogonality Problem in Molecular Quantum Mechanics. *J. Chem. Phys.* **1967**, *47*, 1936.

DOI: 10.1021/jacs.8b08520
J. Am. Chem. Soc. 2018, 140, 17040−17050

(84) Boguslawski, K.; Jacob, C. R.; Reiher, M. Can DFT Accurately Predict Spin Densities? Analysis of Discrepancies in Iron Nitrosyl Complexes. *J. Chem. Theory Comput.* **2011**, *7*, 2740−2752.
(85) Bianchini, C.; Mantovani, G.; Meli, A.; Migliacci, F.; Zanobini, F.; Laschi, F.; Sommazzi, A. Oligomerisation of Ethylene to Linear α-Olefins by new Cs- and C1-Symmetric [2,6-Bis(imino)pyridyl]iron and -cobalt Dichloride Complexes. *Eur. J. Inorg. Chem.* **2003**, *2003*, 1620−1631.
(86) Sur, S. K. Measurement of magnetic susceptibility and magnetic moment of paramagnetic molecules in solution by high-field fourier transform NMR spectroscopy. *J. Magn. Reson.* **1989**, *82*, 169−173.
(87) Bain, G. A.; Berry, J. F. Diamagnetic Corrections and Pascal's Constants. *J. Chem. Educ.* **2008**, *85*, 532−536.
(88) Ciofini, I. DFT calculations of molecular magnetic properties of coordination compounds. *Coord. Chem. Rev.* **2003**, *238−239*, 187−209.
(89) Neese, F. Prediction of molecular properties and molecular spectroscopy with density functional theory: From fundamental theory to exchange-coupling. *Coord. Chem. Rev.* **2009**, *253*, 526−563.
(90) Neese, F.; Wennmohs, F.; Hansen, A.; Becker, U. Efficient, approximate and parallel Hartree-Fock and hybrid DFT calculations. A 'chain-of-spheres' algorithm for the Hartree-Fock exchange. *Chem. Phys.* **2009**, *356*, 98−109.
(91) Neese, F. Software update: the ORCA program system, version 4.0. *Comput. Mol. Sci.* **2018**, *8*, No. e1327.
(92) Pflugrath, J. W. The finer things in X-ray diffraction data collection. *Acta Crystallogr., Sect. D: Biol. Crystallogr.* **1999**, *D55*, 1718.
(93) *CrysAlisPro*; Rigaku Oxford Diffraction, version 171.39.28e, 2017.
(94) *SCALE3 ABSPACK − A Rigaku Oxford Diffraction program for Absorption Corrections*; Rigaku Oxford Diffraction, 2017.
(95) Sheldrick, G. M. SHELXT − Integrated space-group and crystal-structure determination. *Acta Crystallogr., Sect. A: Found. Adv.* **2015**, *A71*, 3.
(96) Sheldrick, G. M. Crystal structure refinement with SHELXL. *Acta Crystallogr., Sect. C: Struct. Chem.* **2015**, *C71*, 3.
(97) Dolomanov, O. V.; Bourhis, L. J.; Gildea, R. J.; Howard, J. A. K.; Puschmann, H. OLEX2: a complete structure solution, refinement and analysis program. *J. Appl. Crystallogr.* **2009**, *42*, 339.
(98) Spek, A. L. Structure validation in chemical crystallography. *Acta Crystallogr., Sect. D: Biol. Crystallogr.* **2009**, *D65*, 148.
(99) Sheldrick, G. M. *Bruker/Siemens Area Detector Absorption Correction Program*; Bruker AXS: Madison, WI, 1998.

DOI: 10.1021/jacs.8b08520
J. Am. Chem. Soc. 2018, 140, 17040−17050